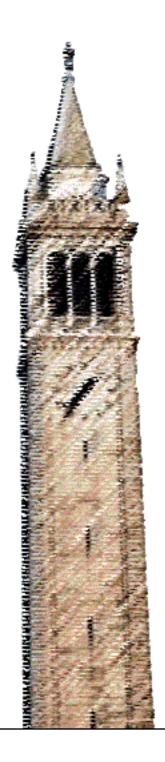# Concentric Rings K-space Trajectory for Hyperpolarized C-13 MR Spectroscopic Imaging

Wenwen Jiang

Electrical Engineering and Computer Sciences
University of California at Berkeley

May 9, 2014

Concentric Ring K-Space Trajectory for Hyperpolarized ^{13}C MR Spectroscopic Imaging

by Wenwen Jiang

Research Project

Submitted to the Department of Electrical Engineering and Computer Sciences, University of California at Berkeley, in partial satisfaction of the requirements for the degree of **Master of Science, Plan II**.

Approval for the Report and Comprehensive Examination:

Committee:

Michael Lustig

Advisor's Name

Research Advisor

2/4/2014

Date

Steve Conolly

Second Reader's Name

Second Reader

1/27/2014

Date

Concentric Rings K-Space Trajectory for Hyperpolarized ^{13}C MR Spectroscopic Imaging

Wenwen Jiang

Will be submitted to *Magnetic Resonance in Medicine* as a Full Paper

Abstract

Purpose: To develop a robust and rapid imaging technique for hyperpolarized ^{13}C MR Spectroscopic Imaging (MRSI) and investigate its performance.

Methods: A concentric rings readout trajectory with constant angular velocity is proposed for hyperpolarized ^{13}C spectroscopic imaging and its properties are analyzed. Quantitative analysis of design tradeoffs are presented for several imaging scenarios in terms of resolution, spectral bandwidth, acquisition time and SNR efficiency. Analysis comparing parallel imaging accelerated Cartesian sampling and concentric rings in terms of reconstruction noise amplification are also presented. Finally, the first application on ^{13}C phantoms and in vivo animal hyperpolarized ^{13}C MRSI studies were performed to demonstrate the feasibility of the proposed method.

Results: The concentric rings MRSI trajectory has the advantages of acquisition timesaving compared to echo-planar spectroscopic imaging (EPSI), and robustness to system timing delay and eddy currents compared to spiral MRSI. It provides a sufficient spectral bandwidth with a relatively high SNR efficiency compared to EPSI and spiral techniques. It will also be beneficial for parallel imaging by reducing noise amplificiation.

Conclusion: The concentric rings trajectory is a robust and rapid imaging technique that fits very well with the speed, bandwidth, and resolution requirements of hyperpolarized ^{13}C MRSI.

Introduction

In vivo detection of ^{13}C labeled substrates by MRSI allows for observation of specific enzyme-catalyzed reactions that reflect altered metabolism in cancer [1]. This was recently made possible by creating hyperpolarized nuclear spins in the liquid state suitable for injection through a process called dissolution dynamic nuclear polarization (DNP). This process greatly improves the signal sensitivity by a factor of 10,000+ [2], thereby allowing the direct monitoring of ^{13}C metabolites in vivo as long as the data acquisition is fast enough to capture the short-lived signal ($\leq$ 1min). The first phase I clinical trial using this technology was recently performed in the Surbeck Laboratory of Advanced Imaging at UCSF, where 31 prostate cancer patients were studied using hyperpolarized ^{13}C MRI. The study showed no adverse effect and demonstrated promising initial imaging results for detecting and staging tumors [3].

Despite these advances, the short-lived effect of hyperpolarization still poses severe challenges for imaging. It is therefore necessary to develop rapid and robust imaging techniques. Furthermore, these techniques must also resolve metabolite signals at multiple resonance frequencies. Techniques have been developed that rely on fast spectroscopic sequences that exploit the most out of the system hardware [4, 5, 6, 7, 8, 9, 10, 11], imaging-based sequences with spectral separation techniques [12, 13, 14], parallel imaging using coil arrays [15, 16, 17], and exploiting structure and redundancy in the data[18, 19].

Fast spectroscopic sequences are advantageous because they provide comprehensive spectral information about all metabolites. This is especially important when using multiple hyperpolarized agents [20] or for agents with more complex spectra such as [1,2-^{13}C] pyruvate [21], which present major design challenges for imaging-based sequences [12, 13, 14]. In comparison to these sequences, fast spectroscopic sequences are also more robust to B0 inhomogeneities.

Currently, both Cartesian (Echo-Planar Spectroscopic Imaging or EPSI [4, 5, 22]) and non-Cartesian (spiral [7, 8, 23] and radial [6] spectroscopic imaging) techniques have been investigated for accelerated hyperpolarized ^{13}C MRSI. EPSI uses bipolar trapezoid magnetic field gradients during signal detection and offers larger k-space coverage. However it suffers from relatively long scan times due

to the number of phase encodings. In addition, minor system imperfections can induce undesirable ghosting artifacts. To prevent ghosting, Flyback EPSI can be used but at the expense of a more limited spectral bandwidth (SBW). This limits the number of metabolites that can be observed without aliasing. Spiral spectroscopic imaging is an alternative that provides a scan-time-efficient imaging scheme, but is highly susceptible to system imperfections (such as gradient timing delay and eddy currents) [24].

To provide scan-time-efficiency and robustness to system imperfections, we propose using concentric rings trajectory (CRT) as the data acquisition method for ^{13}C MRSI. It has the following advantages: I. the acquisition time is halved compared with EPSI, given the same imaging prescriptions; II. the slew rate (a hardware limitation for magnetic field gradients) requirement is less demanding than the time-optimal spiral trajectory; III. CRT is robust to linear eddy currents and system delays; IV. the sampling trajectory results in lower g-factor noise amplification in parallel imaging than EPSI. CRT for MRI was first proposed by Wu *et. al,* [25, 26]. They implemented CRT on magnetization-prepared imaging and corrected for the off-resonance blurring by retracing the central k-space.They also analyzed the unique contrast and robustness properties of CRT. Later, Kwon *et. al* [27] implemented the concentric cylinders trajectory on 3D magnetization-prepared imaging. In their study, Kwon *et. al,* demonstrated the feasibility of the 3D concentric cylinder for magnetization-prepared imaging. In another recent work, Furuyama *et. al,* [28] implemented CRT in a standard PRESS based spectroscopy sequence for proton MRSI. They demonstrated feasibility in the healthy human brain in vivo, taking advantage of the trajectory robustness and two-fold acceleration over EPSI. None of these works have reported quantitative comparisons between CRT and other MRSI trajectories to evaluate resolution, spectral bandwidth and SNR efficiency. Moreover, for the hyperpolarized ^{13}C MRSI application, some practical challenges and unique properties which are well-suited to CRT have not been exploited yet.

In this work, we demonstrate the efficacy of CRT through a quantitative comparison between CRT, EPSI and spiral MRSI, and a hyperpolarized ^{13}C MRSI CRT sequence which was used for ^{13}C phantom and hyperpolarized ^{13}C in vivo animal applications. We also extended the analysis of CRT to parallel imaging for additional acceleration.

Methods

Concentric Rings Trajectory Design for MRSI

Our CRT for MRSI is derived similarly as in [25, 26]. Gradients are designed for the outermost ring with respect to the spatial resolution and spectral bandwidth (SBW) and then scaled down for the inner rings with the readout window $T_{readout}$ kept constant. We use CRT with constant angular velocity since they are robust to timing and eddy currents delays. The radius of the outermost ring is set according to the desired spatial resolution. Maximum gradient amplitude and slew rates set an upper limit on the achievable spectral bandwidth. The spectral bandwidth is determined by the retracing period ΔT. The number of rings N_{ring} determines the in-plane field of view (FOV), whereas the number of revolutions N_{rev} determines the spectral resolution – which is ultimately limited by T_2^* decay.

The prewinders and rewinders are designed using the time-optimal gradient design by Hargreaves *et. al,* [29] and implemented in Matlab (The Mathworks, Natick MA, USA.) and the CVX [30] convex optimization toolbox. The trajectory for an axial plane is shown in Figure 1.

The constant angular velocity of rings is insensitive to some system imperfections. Timing and eddy currents induced delays result in benign rotations of images [26, 27] rather than spatial blurring.
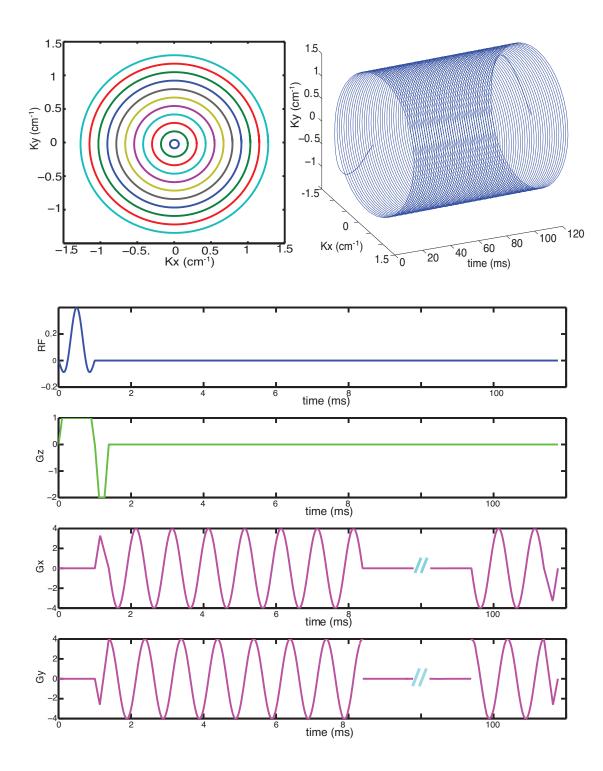
Figure 1: Concentric rings trajectory and sequence design: top-left shows the spatial concentric rings k-space trajectory; top-right shows the spatial and spectral k-space trajectory; bottom shows the concentric rings GRE sequence for axial images

Comparison of the Concentric Rings Trajectory with EPSI and Spiral

For MRSI sequences, especially in hyperpolarized studies, optimizing the total scan time, spectral bandwidth, and SNR is crucial for capturing the intrinsic contrast and biochemical information. A quantitative study of CRT using these key parameters was performed in order to compare against three other commonly used MRSI schemes: EPSI (both symmetric and flyback EPSI) and spiral spectroscopic trajectories. Figure 2 illustrates the k-space trajectories for the different methods. In symmetric EPSI k-space is scanned in a zigzag trajectory and is collected in both directions (green and yellow arrows in the symmetric EPSI in Fig. 2). In our analysis we compare against a design in which the spectral bandwidth is determined by the time between scans in the same direction, *e,g,* between green arrows. This guarantees Nyquist sampling of the spectrum and is the preferred method in the hyper polarized ^{13}C community. We refer to this approach as Nyquist-Constrained symmetric EPSI[5]. However, it is possible to exploit Papoulis's generalized sampling theory and double the spectral bandwidth of the current symmetric design, as it was initially implemented in proton MRSI. In this situation the spectral BW is defined by the time between alternate scanning directions, *e.g. between green and yellow arrows.* We refer to this approach as as "critical symmetric EPSI". We elaborate on this approach in the Reconstruction and Data Processing section.

For a fair comparison, we fixed some specific prescriptions when evaluating acquisition time, SBW and SNR efficiency with respect to the spatial resolution. The parameter range were chosen according to typical routine hyperpolarized pre-clinical prescriptions for [1-^{13}C]pyruvate that are performed in our institution: FOV $= 16 \times 16$ cm^2, spectral resolution $= 10$ Hz (*i.e.,* the readout window $T_{readout} = 100$ ms), spatial resolution is in the range from 0.36 cm to 1 cm. All designs assume a gradient amplitude limit of 40 mT/m and maximum slew rate of 150 mT/m/ms.
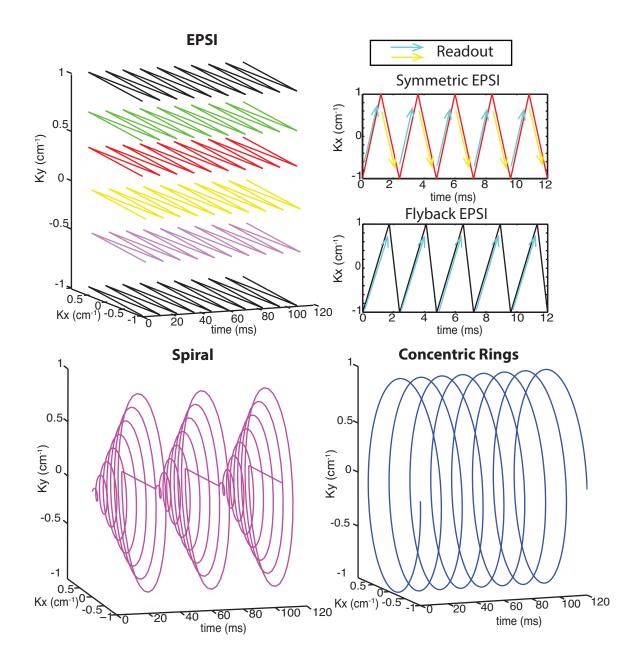
6

Figure 2: K-space trajectories of EPSI, spiral and concentric rings spectroscopic imaging; the arrows illustrates the readout window for both symmetric EPSI and flyback EPSI; for symmetric EPSI, we use different-colored arrows to differentiate the odd/even retracing lines for reconstruction.

Acquisition Time Comparison

The acquisition time should be as short as possible to "freeze" the ^{13}C signal while hyperpolarized compounds undergo metabolic conversion and before they decay back to equilibrium. For comparing acquisition time we fixed the SBW = 500 Hz, TR = 200 ms, spectral resolution = 10 Hz and FOV = 16×16 cm^2. The total acquisition time $\mathrm{T_{acquisition\ time}}$ is simply the product of TR, the number of phase encodings $\mathrm{N_{pe}}$ and the number of interleaves in time $\mathrm{N_{interleaves}}$.

$$T_{\text{acquisition time}} = TR \times N_{\text{pe}} \times N_{\text{interleaves}} \tag{1}$$

SNR Efficiency Comparison

In our SNR efficiency comparisons we fixed some parameters: SBW = 500 Hz, spectral resolution = 10 Hz and FOV = 16×16 cm^2. We considered the duty cycle and the k-space sampling uniformity effects on SNR efficiency. (We do not consider T1 effects and the number of excitations. Unlike conventional imaging, hyperpolarized ^{13}C imaging often uses a progressive flip angle [31], which equalizes the magnetization for each excitation. This results in an SNR that is independent of the number of excitations and this is elaborated in the following parallel imaging with concentric rings section. Since relatively small number of excitations are considered here, T1 effects can be neglected. When the acquisition is long, T1 decay during the scan will reduce the available magnetization. It's worth mentioning that spirals and rings will have the advantage over EPSI since they require less acquisitions.)

SNR efficiency depends on the duty cycle:

$$SNR_{\text{eff,duty}} = \sqrt{\frac{T_{\text{active time}}}{T_{\text{readout}}}}, \tag{2}$$

where $\mathrm{T_{active\ time}}$ is the total duration of the active readout gradients while $\mathrm{T_{readout}}$ is the duration of readout window.

It is also dependent on the uniformity of the sampling trajectory. Non-uniform sampling acquisitions

are less SNR efficient than uniform ones. This was nicely demonstrated in [32], where the effective SNR efficiency is given by:

$$SNR_{\text{eff,uniformity}} = \frac{A_k}{\int_{\vec{k}} D(\vec{k})\, d\vec{k} \int_{\vec{k}} \frac{1}{D(\vec{k})} d\vec{k}},\tag{3}$$

where $D(\vec{k})$ is the density of the corresponding sampling position, and A_k is the k-space coverage.

We define the overall SNR efficiency to be the product of the above two formulas and compute the SNR efficiency for different trajectories.

For flyback and symmetric EPSI, we are required to use ramp sampling (as otherwise the SBW requirement is not achievable). For the spiral trajectory, we designed constant slew rate spiral trajectories for different imaging resolution in order to minimize the total acquisition time, which is essential for hyperpolarized ^{13}C imaging.

Spectral Bandwidth

Spectral bandwidth (SBW) relates to the number of metabolites we can observe without spectral aliasing. For example, in hyperpolarized [1-^{13}C]pyruvate studies at 3T, 500 Hz SBW is a reasonable range to display the pyruvate and the products of [1-^{13}C]lactate and [1-^{13}C]alanine. Here we fixed spectral resolution = 10 Hz spectral resolution and FOV = 16×16 cm^2. SBW is determined by ΔT, which is the retracing period (in Equation 4) to the same k-space position.

$$SBW = \frac{1}{\Delta T}\tag{4}$$

Parallel Imaging with Concentric Rings

Parallel imaging is favorable for hyperpolarized ^{13}C imaging because the shorter scan times reduce SNR losses due to T1 decay and metabolism during the acquisition. In non-hyperpolarized imaging, undersampling of k-space in parallel imaging reduces the acquisition time but at the trade-off of

losing SNR, as Equation 5 shows [33]

$$SNR_{und} = \frac{SNR_{full}}{g\sqrt{R}}$$

(5)

SNR_{und} and SNR_{full} are the undersampled and fully sampled SNR respectively, and R is the acceleration factor. The G factor, g, is spatially variant noise enhancement that depends on the receiver coil array and sampling pattern.

However, the inherent signal of hyperpolarized ^{13}C imaging is limited. With undersampling, the given amount of total magnetization can be distributed into fewer excitations where each excitation has more signal. In fact, reduced acquisition times may translate into higher image SNR due to the reduced T1 relaxation [15]. As a result, parallel imaging does not result in losing inherent signal if a progressive flip angle [31] is applied (shown in Equation 6). This results in an undersampled SNR of

$$SNR_{und} = \frac{SNR_{full}}{g}.$$

(6)

Given the same phase-array coil sensitivity, the G-factor is determined by the sampling pattern. A Monte-Carlo technique, which is also known as pseudo replica method [34], was used to calculate g-factor maps of a simulated 8-channel phased-array coil and 4-fold undersampling with CRT and rectilinear Cartesian (*i.e.,* EPSI) trajectories. Fully encoded series of images with identical parameters was simulated. Out of this image series, an SNR_{full} map of the fully encoded image can be derived by taking the mean and the standard deviation on a pixel-by-pixel basis throughout the image series. Undersampling was achieved by uniformly skipping phase encodings for both CRT and Cartesian counterparts. Similarly, after reconstruction an SNR_{und} map of under sampled encoded image can be generated and a g-factor map is computed by the Equation 5.

The g-factor maps were 256× 256 and cropped to display circular FOV. CRT's g-factor maps were generated by using fully sampled 128 rings and undersampled 32 rings respectively, while the Cartesian (EPSI) g-factor map was generated by fully sampled 256 phase encodings and undersampled 64 phase encodings. We used conjugate gradient SENSE (CG-SENSE) [35] without regularization for the reconstruction. The number of pseudo replicas is 50 for both sampling patterns.

Sequence Design Parameters for Concentric Rings Trajectory

CRT was implemented into the readout window of a gradient echo (GRE) 2D slice-selective pulse sequence. The spectroscopic imaging module consists of readout window duration $T_{readout} = 100$ ms, corresponding to a spectral resolution of $\Delta f = 10$ Hz, and a SBW = 500Hz, which sets the duration of each revolution to $\Delta T = 2$ms. The in-plane isotropic spatial resolution was 3.67mm, which is limited by the slew rate and by the SBW. For the ^{13}C phantom study, the flip angle (FA) was set to be constant for each excitation. In the hyperpolarized studies, a progressive flip angle technique [31] was applied in order to equalize the signal across excitations. Temporal interleaves were implemented by rotation of the readout trajectory in order to increase spectral bandwidth, and this is also one specific difference for CRT compared with EPSI.

Experiments   All the phantom and in vivo studies were conducted on a 3.0 T GE clinical scanner (GE Healthcare, Waukesha, WI) with maximum gradient amplitude of 40 mT/m and maximum slew rate of 150 mT/m/ms. All the animal studies conducted were approved by our Institutional Animal Care and Use Committee (IACUC).

Hyperpolarized ^{13}C in vivo Spectroscopic Imaging

In vivo experiments were performed on rats. For all the rats, a tail vein catheter was placed immediately before the hyperpolarized MR study. Next, the anesthetized rats were placed on a water-filled, temperature-controlled pad that was heated to approximately 37 C° and positioned inside of the coil.

Initially, T_2-weighted ^{1}H anatomic MR images were acquired in sagittal, axial, and coronal views. The subsequent hyperpolarized ^{13}C scans were prescribed on the chosen slices. A mixture of [1-^{13}C] pyruvic acid and the trityl radical (tris methyl sodium salt; GE Healthcare) was polarized using the HyperSense polarizer (Oxford Instruments, Oxford, UK). After the mixture was polarized, it was rapidly dissolved into a pH-balanced Tris buffer solution targeting a hyperpolarized 100 mmol/L pyruvate solution with a neutral pH. Next, the solution was quickly transported to the MR scanner and 2.2 mL was injected into the rat over 12 s. The imaging data acquisition was initiated 30 s after

the start of the pyruvate injection to coincide with the peak lactate signal. A slice-selective pulse sequence with a variable flip angle excitation pulse using CRT was performed using a TE/TR = 3.4/200 ms, readout window $T_{readout} = 100$ ms, and 11 rings. Additional sequence prescriptions for rat studies include: FOV= 8×8 cm^2, slice thickness of 10 mm, resolution = 3.8×3.8 mm^2, and 500 Hz SBW. The data was reconstructed by 3D gridding and spatially zero padded to be a $44 \times 44 \times 50$ matrix. The total scan time was 2.2 s. For this study, the total scan time could be reduced by 35% by decreasing TR.

Reconstruction and Data Processing

Image reconstruction and postprocessing were carried out in Matlab. We applied density compensation to the non-Cartesian raw data, 3D gridded it into Cartesian data, and then performed an FFT. Gridding and FFT were done by using Fessler's non-uniform fast Fourier transform (NUFFT) toolbox [36] with min-max Kaiser-Bessel kernel interpolation and twice oversampling. The matrix size of the reconstructed CRT image after 3D gridding (2D spatial + 1D spectral) was $2N_{ring} \times 2N_{ring} \times N_{rev}$. The same reconstruction method is also applicable for symmetric EPSI (Nyquist-constrained) and flyabck EPSI. For parallel imaging, iterative SENSE [35] reconstruction and Monte-Carlo method were performed to compute the g-factor maps.

Critical Symmetric EPSI Reconstruction

Currently, the Nyquist-constrained symmetric EPSI reconstruction is to separate the odd and even numbered retracing lines, perform the inverse Fourier transform separately and average the separate signals for better SNR [5]. But this kind of design and reconstruction over prescribes the SBW, while not critically using up the sampling limits. Papoulis's generalized sampling theory [39] asserts that in some cases aliasing artifact-free signals can be reconstructed even if the Nyquist criterion is violated in some regions of the Fourier domain.

As is explicitly demonstrated in [40, 41], critical symmetric EPSI reconstruction can be regarded as a matrix inversion problem that even if the Nyquist criterion is violated in some regions of the

spectral domain, but at the cost of noise amplification.

In Figure 3, we demonstrate the symmetric EPSI reconstruction algorithm. Here we only plot the Kx-t joint domain since Ky (phase encoding direction) is uniform. Basically, the critical design of symmetric EPSI trajectory is to make sure the temporary sampling rate at Kx = 0 fulfills Nyquist rate of the required spectral bandwidth (as the black star in Figure 3). Regarding to the non-uniform samples, each Kx_i's non-uniformity is different, with different delay Δt_i. We separate the odd/even retracing lines based on the labels. For odd or even lines respectively, they are uniformly sampled but at the rate of 2/SBW. We apply 1D inverse Fourier Transform in temporary domain to odd and even numbered retracing lines separately. The difference between odd and even lines reconstruction is the linear phase combination (due to the delay in the sampling domain). Then, we apply the matrix inversion to recover the full spectra as shown in the following equation.

The noise amplification is resulting from inverting the matrix

$$\begin{pmatrix} 1 & 1 \\ 1 & e^{i\Delta t_i * SBW\pi} \end{pmatrix}$$, and it is shown in Figure 3 by color bar (as neatly explained in [40]).
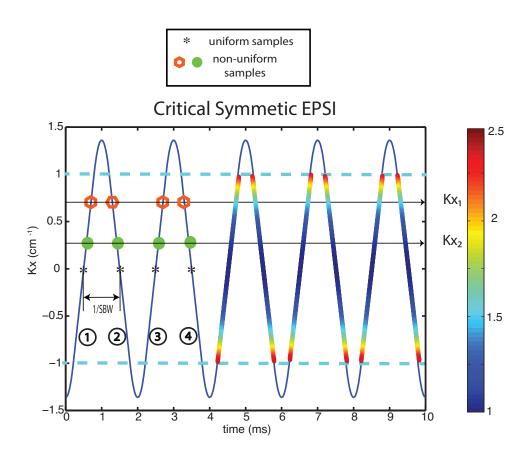
Figure 3: EPSI Recontruction: The area between the light blue dashed lines is the k-space used for the reconstruction; red and green samples are non-uniform Kx_i, samples in temporal domain. With the above method we described, the SBW could be doubled but at the cost of noise amplifcation.The colorbar indicated the noise amplification at different Kx_i.

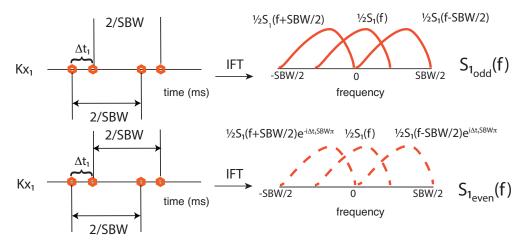For example, we now exam a single k-space point at the Kx_1 as Figure 4.

Figure 4: At Kx_1, we separate odd and even samples at each retracing lines and perform 1DFT respectively. Then we will see the spectral replica resulting from both odd and even lines reconstruction. But there is a phase shift between the odd and even samples, which determines the inversion matrix.

The time interval between the odd and even data points (Δt_1) is not equal to the interval between the even and the odd points ($T - \Delta t_1$) and is dependent on Kx_1; However, the time between odd(or even) points, T (*i.e.,* the prescribed 2/SBW), is a constant and independent on Kx_1. The interval $0 \leq f \leq SBW/2$ spectrum $S_1(f)$ can be recovered by the matrix inversion of the following equation:

$$\begin{pmatrix} 1 & 1 \\ 1 & e^{i\Delta t_1 * SBW\pi} \end{pmatrix} \begin{pmatrix} S_1(f) \\ S_1(f - SBW/2) \end{pmatrix} = \begin{pmatrix} S_{1odd}(f) \\ S_{1even}(f) \end{pmatrix}$$

The interval $-SBW/2 \leq f \leq 0$ spectrum $S_1(f)$ can be recovered by the matrix inversion of the similar equation:

$$\begin{pmatrix} 1 & 1 \\ 1 & e^{-i\Delta t_1 * SBW\pi} \end{pmatrix} \begin{pmatrix} S_1(f) \\ S_1(f + SBW/2) \end{pmatrix} = \begin{pmatrix} S_{1odd}(f) \\ S_{1even}(f) \end{pmatrix}$$

Due to the different delay Δt_i, the linear phase compensation is different for Kx_i. After we apply the appropriate phase compensation to all the Kx_i, 2D inverse Fourier Transform is applied on Kx-Ky domain to reconstruct the whole spatial-spectral signal.

With this reconstruction method, we could exploit the intrinsic SBW by a factor of two with current Nyquist-constrained symmetric EPSI waveforms. So the SBW analyses from Figure 5 could be doubled for symmetric EPSI. However, we have to notice that the noise amplification of the matrix inversion could be large depending on the non-uniformity of delay Δt_i at different Kx_i. At larger Kx, that is for higher resolution, the condition worsens and the penalty is the higher sensitivity to noise. The overall noise amplification is the summation of the noise amplification at all the Kx coordinates as the plot shows. The finer the resolution, the larger noise amplification is. In addition, the precise coordinates of sampled data are important for image reconstruction using the this technique.

Results

Comparison of the Concentric Rings Trajectory with EPSI and Spiral

In the following, we compared CRT with EPSI and spiral MRSI trajectories in terms of resolution, acquisition time, SNR efficiency, and spectral bandwidth.

Acquisition Time

As shown in Figure 5 (top-left), since both symmetric EPSI and flyback EPSI have the same number of phase encoding and interleaves are not required, they result in the same total acquisition time for each individual resolution. Compared with EPSI, CRT requires fewer phase encodings and no interleaves, so it results in saving half of the total acquisition time given the same TR. For the spiral trajectory design, we used a constant slew rate spiral in order to optimize the gradient duration and required interleaving of the spiral trajectory to fulfill the spectral bandwidth requirement (500 Hz). Spirals are the most time efficient of all the trajectories, while CRTs are twice as fast as EPSI trajectories.

SNR Efficiency

Figure 5 (top-right) shows the SNR efficiency of different trajectories with various resolution prescriptions. The SNR loss for flyback EPSI is mostly due to its low duty cycle. The finer the resolution is, the lower the duty cycle will be and SNR efficiency goes lower as the flyback portion requires more time. Though the duty cycle for symmetric EPSI is 100% (including ramp sampling), the non-uniform k-space sampling resulting from the ramp part of the trapezoid waveform reduces the SNR efficiency to some extent. The SNR efficiency is very high for symmetric EPSI but not 100%. As the resolution gets coarser, the ramp portion is smaller, so the SNR efficiency is higher. For the constant slew rate spiral trajectories, the SNR efficiency decreases as the resolution becomes coarser with a fixed FOV since there is proportionally less outer k-space sampling where spirals are more uniform than inner k-space. And non-uniformity results in the most of the SNR loss of spirals while duty cycle results in a smaller fraction of the loss. Benefiting from the design of constant slew rate, the spiral trajectories provide even better SNR efficiency than flyback EPSI and CRT. CRT offers a constant SNR efficiency of $\frac{\sqrt{3}}{2}$, which is better than flyback EPSI with the chosen prescriptions. The loss of SNR efficiency for CRT is caused by the non-uniformity.

Spectral Bandwidth

EPSI traverses a rectilinear line in k-space for each retracing period, CRT traverses a circle, while spiral traverses the whole spatial k-space in each period. Given the same traversing velocity (determined by the gradient waveforms), accordingly, the achieved SBW for EPSI, CRT, and spirals are decreasing in order, as shown in Figure 5 (bottom-left) without interleaves. To exploit the maximum spectral bandwidth, both symmetric EPSI and flyback EPSI result in the same waveform design thus achieving the same spectral bandwidth. They are only slightly better than CRT since flyback EPSI requires flyback time and symmetric EPSI (Nyquist constrained) does not critically exploit the whole spectral bandwidth.

However, CRT and spiral trajectories are more scan-time-efficient compared with EPSI. If we take advantage of scan-time-efficiency by applying interleaves in temporal domain, we can increase

SBW. In Figure 5 (bottom-right), the SBW of all trajectories was computed by accounting for the interleaves in time domain constrained for the same total acquisition time. Considering this tradeoff, spiral trajectories offer the best SBW, while CRT's spectral bandwidth is doubled compared to EPSI. The non-monotonicity of the spiral trajectories SBW with respect to resolution in this analysis is due to using an integer number of interleaves.

Simulation of Parallel Imaging with the Concentric Rings

As the g-factor maps (in Figure 6) confirm, the non-rectilinear circular sampling pattern of CRT results in more incoherent noise amplification than Cartesian counterparts such as EPSI. Noise is amplified by 3-4 times at more discrete locations for the Cartesian undersampling pattern due to the worse conditioning. For CRT, the noise is more uniformly distributed spatially, resulting in a noise amplification of no more than 2.5 for this simulated 8-channel array with $4\times$ under-sampling. (In conjunction with appropriate regularization, the g-factor can be further improved.) The non-Cartesian sampling pattern of concentric rings is advantageous because it makes the noise amplification incoherent thus lowering the g-factor of the whole space.

Hyperpolarized ^{13}C In Vivo Spectroscopic Imaging with Concentric Rings

The imaging plane was chosen at the abdomen of rat in axial view (in Figure 7). The kidneys of rats showed the high uptake of pyruvate and its conversion to alanine and lactate. Spatially, the structure of kidneys and arteries along with metabolic conversion were captured.
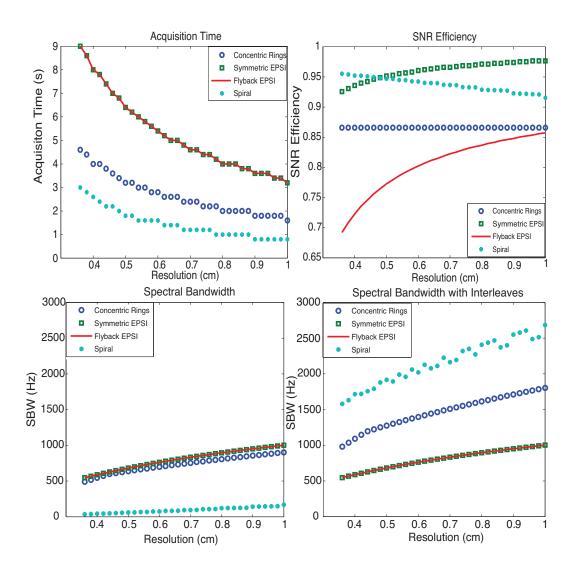
Figure 5: Comparison of concentric rings, EPSI and spiral spectroscopic imaging: top-left shows the acquisition time; top-right shows the SNR efficiency; bottom-left and bottom-right show the SBW and SBW with spectral interleaves. CRT requires half of the total acquisition time compared with EPSI trajectories, offers about 87% SNR efficiency, and provides much wider spectral bandwidth than flyback EPSI and symmetric EPSI. Although nominally spirals are the most efficient trajectories, offering the best acquisition time and spectral bandwidth benefit while sacrificing the least SNR, they are limited by susceptibility to gradient infidelities.
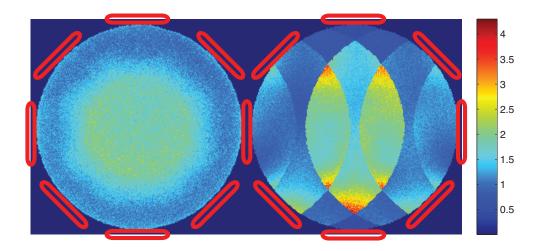
Figure 6: G-factor map of 4× undersampled concentric rings trajectory (on the left) and Carteisan trajectory counterpart, such as EPSI, (on the right) for a simulated 8-channel array. The isotropic non-Cartesian undersampling pattern of the concentric rings trajectory results in less coherent noise amplification than the Cartesian counterpart.
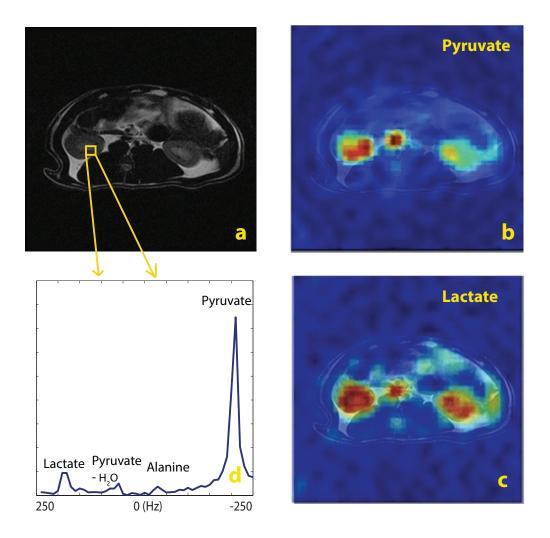
Figure 7: In vivo results using concentric rings in a normal rat (axial): a. ^{1}H T_2-weighted localizer; b. [1-^{13}C] pyruvate image; c. [1-^{13}C] lactate image; d. the ^{13}C spectrum of a selected voxel with 500 Hz SBW. MRSI was acquired with a spatial resolution of $3.8{\times}3.8$ mm^2. Pyruvate image and lactate images were zero filled to have a resolution of $1.9{\times}1.9$ mm^2. For display purposes, the intensity of lactate image was scaled up by 7. The total scan time was 2.2 s.

Discussion

CRT provides a competitive alternative to ^{13}C existing spectroscopic imaging acquisition methods. Our CRT sequence requires half the number of excitations compared to EPSI. This has an advantage in two-fold acquisition time savings. In addition, the T1 decay is reduced, which leads to overall higher SNR [15]. The acquisition time saving can be traded off for an increased spectral bandwidth through interleaving. We also showed that even though CRT samples k-space non-uniformly, its SNR efficiency is still $\frac{\sqrt{3}}{2} \approx 0.87$ of uniform sampling.

Unlike spiral or critical EPSI, the concentric rings trajectory is robust to system imperfections. Any gradient timing delay or eddy currents will results in some artifacts. In spirals, delays cause spatial blurring. In critical EPSI, the effect is odd-even echo inconsistency which results in spectral aliasing. This is analogous to ghosting artifacts in EPI [37]. For CRT, simple delays are translated to benign image rotations. More importantly, no spectral aliasing is observed with appropriate prescriptions.

One of the advantages of using CRT is robustness to flow that was also reported in [25]. Pulsatile flow is blurred by CRT. In contrast, EPSI trajectories can suffer from significant pulsatile flow artifacts where flow results in replicas in phase encoding direction.

Combining CRT with parallel imaging for hyperpolaizated ^{13}C imaging is also very promising. Undersampling is achieved by acquiring fewer rings than what are necessary for in plane full-FOV. We showed in Monte Carlo simulations that with CRT the resulting g-factor due to undersampling is lower than for Cartesian undersampling. The reason is that CRT undersamples isotropically in-plane, whereas Cartesian imaging can accelerate only in the phase-encoding directions. As a result, CRT acquisitions can better utilize the multi-dimensional spatial variation of the coils sensitivities to improve the conditioning of the reconstruction. Furthermore, for hyperpolaized ^{13}C we do not suffer from the usual $\sqrt{R}$ loss of SNR due to subsampling. The reason is that the total magnetization can be redistributed optimally to fewer number of excitations. Hyperpolarized ^{13}C parallel imaging with CRT is essential for the large FOV applications, *e.g.,* metastatic cancer imaging.

There are some possible extensions of CRT for ^{13}C MRSI: (1) the shorter scan time could be amortized for dynamic MRSI to track perfusion and metabolism kinetics; (2) 3D MRSI to cover a larger volume in vivo; (3) variable-density undersampling designs for parallel imaging, maintaining the inner k-space fully sampled to capture the intrinsic contrast and outer k-space undersampled for resolution and acceleration; (4) compressed sensing, taking advantages of intrinsically sparse ^{13}C spectra [18, 19]. These improvements could further reduce the total scan time.

Conclusion

Our preclinical studies have demonstrated the potential and feasibility of using concentric rings in hyperpolarized ^{13}C MRSI for a two-fold acceleration over EPSI, with inherent robustness to flow artifacts, gradient system delay and eddy currents. Parallel imaging will also benefit from this trajectory for hyperpolarized ^{13}C imaging. Compared with existing methods, the concentric rings trajectory provides flexible and robust trade-off between acquisition time and spectral bandwidth, thereby acting as an effective alternative for hyperpolarized ^{13}C MRSI .

Acknowledgement

References

[1] Kurhanewicz J, Vigneron DB, Brindle K, Chekmenev EY, Comment A, Cunningham CH, DeBerardinis RJ, Green GG, Leach MO, Rajan SS et al. Analysis of cancer metabolism by

imaging hyperpolarized nuclei: prospects for translation to clinical research. Neoplasia (New York, NY) 2011; 13:81.

[2] ArdenkjærLarsen JH, Fridlund B, Gram A, Hansson G, Hansson L, Lerche MH, Servin R, Thaning M, Golman K. Increase in signal-to-noise ratio of $> 10,000$ times in liquid-state nmr. Proceedings of the National Academy of Sciences 2003; 100:10158–10163.

[3] Nelson SJ, Kurhanewicz J, Vigneron DB, Larson PEZ, Harzstark AL, Ferrone M, van Criekinge M, Chang JW, Bok R, Park I, Reed G, Carvajal L, Small EJ, Munster P, Weinberg VK, ArdenkjaerLarsen JH, Chen AP, Hurd RE, Odegardstuen LI, Robb FJ, Tropp J, Murray JA. Metabolic imaging of patients with prostate cancer using hyperpolarized [1-13c]pyruvate. Science Translational Medicine 2013; 5:198ra108.

[4] Cunningham CH, Vigneron DB, Chen AP, Xu D, Nelson SJ, Hurd RE, Kelley DA, Pauly JM. Design of flyback echo-planar readout gradients for magnetic resonance spectroscopic imaging. Magnetic resonance in medicine 2005; 54:1286–1289.

[5] Yen YF, Kohler S, Chen A, Tropp J, Bok R, Wolber J, Albers M, Gram K, Zierhut M, Park I, Zhang V, Hu S, Nelson S, Vigneron D, Kurhanewicz J, Dirven H, Hurd R. Imaging considerations for in vivo 13c metabolic mapping using hyperpolarized 13c-pyruvate. Magnetic Resonance in Medicine 2009; 62:1–10.

[6] Ramirez MS, Lee J, Walker CM, Sandulache VC, Hennel F, Lai SY, Bankson JA. Radial spectroscopic mri of hyperpolarized [1-(13) c] pyruvate at 7 tesla. Magn Reson Med 2013; .

[7] Mayer D, Levin YS, Hurd RE, Glover GH, Spielman DM. Fast metabolic imaging of systems with sparse spectra: application for hyperpolarized 13C imaging. Magn Reson Med 2006; 56:932–7.

[8] Josan S, Hurd R, Park JM, Yen YF, Watkins R, Pfefferbaum A, Spielman D, Mayer D. Dynamic metabolic imaging of hyperpolarized [2-(13) c]pyruvate using spiral chemical shift imaging with alternating spectral band excitation. Magn Reson Med 2013; .

[9] Leupold J, Månsson S, Petersson JS, Hennig J, Wieben O. Fast multiecho balanced ssfp metabolite mapping of (1)h and hyperpolarized (13)c compounds. MAGMA 2009; 22:251–6.

[10] Wiesinger F, Weidl E, Menzel MI, Janich MA, Khegai O, Glaser SJ, Haase A, Schwaiger M, Schulte RF. Ideal spiral csi for dynamic metabolic mr imaging of hyperpolarized [1-13c]pyruvate. Magn Reson Med 2012; 68:8–16.

[11] Gordon JW, Niles DJ, Fain SB, Johnson KM. Joint spatial-spectral reconstruction and k-t spirals for accelerated 2d spatial/1d spectral imaging of (13) c dynamics. Magn Reson Med 2013; .

[12] von Morze C, Reed G, Shin P, Larson PEZ, Hu S, Bok R, Vigneron DB. Multi-band frequency encoding method for metabolic imaging with hyperpolarized [1-(13)c]pyruvate. J Magn Reson 2011; 211:109–113.

[13] Lau AZ, Chen AP, Ghugre NR, Ramanan V, Lam WW, Connelly KA, Wright GA, Cunningham CH. Rapid multislice imaging of hyperpolarized 13c pyruvate and bicarbonate in the heart. Magn Reson Med 2010; 64:1323–31.

[14] Cunningham CH, Chen AP, Lustig M, Hargreaves BA, Lupo J, Xu D, Kurhanewicz J, Hurd RE, Pauly JM, Nelson SJ, Vigneron DB. Pulse sequence for dynamic volumetric imaging of hyperpolarized metabolic products. J Magn Reson 2008; 193:139–146.

[15] Arunachalam A, Whitt D, Fish K, Giaquinto R, Piel J, Watkins R, Hancu I. Accelerated spectroscopic imaging of hyperpolarized c-13 pyruvate using sense parallel imaging. NMR in Biomedicine 2009; 22:867–873.

[16] Tropp J, Lupo JM, Chen AP, Calderon P, McCune D, Grafendorfer T, OzturkIsik E, Larson PE, Hu S, Yen YF, Robb F, Bok R, Schulte R, Xu D, Hurd R, Vigneron D, Nelson S. Multi-channel metabolic imaging, with sense reconstruction, of hyperpolarized [1-13c] pyruvate in a live rat at 3.0 tesla on a clinical mr scanner. J Magn Reson 2011; 208:171–177.

[17] Ohliger MA, Larson PEZ, Bok RA, Shin P, Hu S, Tropp J, Robb F, Carvajal L, Nelson SJ, Kurhanewicz J, Vigneron DB. Combined parallel and partial fourier mr reconstruction for accelerated 8-channel hyperpolarized carbon-13 in vivo magnetic resonance spectroscopic imaging (mrsi). J Magn Reson Imaging 2013; 38:701–13.

[18] Larson PEZ, Hu S, Lustig M, Kerr AB, Nelson SJ, Kurhanewicz J, Pauly JM, Vigneron DB. Fast dynamic 3d mr spectroscopic imaging with compressed sensing and multiband excitation pulses for hyperpolarized 13c studies. Magn Reson Med 2011; 65:610–9.

[19] Hu S, Lustig M, Balakrishnan A, Larson PEZ, Bok R, Kurhanewicz J, Nelson SJ, Goga A, Pauly JM, Vigneron DB. 3d compressed sensing for highly accelerated hyperpolarized 13c mrsi with in vivo applications to transgenic mouse models of cancer. Magnetic Resonance in Medicine 2010; 63:312–321.

[20] Wilson DM, Keshari KR, Larson PEZ, Chen AP, Criekinge MV, Bok R, Nelson SJ, Macdonald JM, Vigneron DB, Kurhanewicz J. Multi-compound polarization by dnp allows simultaneous assessment of multiple enzymatic activities in vivo. J Magn Reson 2010; 205:141–147.

[21] Chen AP, Hurd RE, Schroeder MA, Lau AZ, Gu Yp, Lam WW, Barry J, Tropp J, Cunningham CH. Simultaneous investigation of cardiac pyruvate dehydrogenase flux, krebs cycle metabolism and ph, using hyperpolarized [1,2-13c2]pyruvate in vivo. NMR Biomed 2012; 25:305–311.

[22] Mansfield P. Spatial mapping of the chemical shift in nmr. Magn Reson Med 1984; 1:370–86.

[23] Adalsteinsson E, Irarrazabal P, Topp S, Meyer C, Macovski A, Spielman DM. Volumetric spectroscopic imaging with spiral-based k-space trajectories. Magnetic resonance in medicine 1998; 39:889–898.

[24] Kim DH, Spielman DM. Reducing gradient imperfections for spiral magnetic resonance spectroscopic imaging. Magnetic Resonance in Medicine 2006; 56:198–203.

[25] Wu HH, Lee JH, Nishimura DG. Mri using a concentric rings trajectory. Magnetic Resonance in Medicine 2008; 59:102–112.

[26] Wu HH. "MAGNETIC RESONANCE IMAGING USING A CONCENTRIC RINGS K-SPACE TRAJECTORY". PhD thesis, Stanford University, September 2009.

[27] Kwon KT, Wu HH, Shin T, Çukur T, Lustig M, Nishimura DG. Three-dimensional magnetization-prepared imaging using a concentric cylinders trajectory. Magnetic Resonance in Medicine 2013; pp. n/a–n/a.

[28] Furuyama JK, Wilson NE, Thomas MA. Spectroscopic imaging using concentrically circular echo-planar trajectories in vivo. Magnetic Resonance in Medicine 2012; 67:1515–1522.

[29] Hargreaves BA, Nishimura DG, Conolly SM. Time-optimal multidimensional gradient waveform design for rapid imaging. Magnetic resonance in medicine 2004; 51:81–92.

[30] CVXResearch I. CVX: Matlab software for disciplined convex programming, version 2.0. http://cvxr.com/cvx, August 2012.

[31] Zhao L, Mulkern R, Tseng CH, Williamson D, Patz S, Kraft R, Walsworth RL, Jolesz FA, Albert MS. Gradient-echo imaging considerations for hyperpolarized ^{129} xe mr. Journal of Magnetic Resonance, Series B 1996; 113:179–183.

[32] Tsai CM, Nishimura DG. Reduced aliasing artifacts using variable-density k-space sampling trajectories. Magnetic resonance in medicine 2000; 43:452–458.

[33] Pruessmann KP, Weiger M, Scheidegger MB, Boesiger P. Sense: Sensitivity encoding for fast mri. Magnetic Resonance in Medicine 1999; 42:952–962.

[34] Breuer FA, Kannengiesser SA, Blaimer M, Seiberlich N, Jakob PM, Griswold MA. General formulation for quantitative g-factor calculation in grappa reconstructions. Magnetic Resonance in Medicine 2009; 62:739–746.

[35] Pruessmann KP, Weiger M, Börnert P, Boesiger P. Advances in sensitivity encoding with arbitrary k-space trajectories. Magnetic Resonance in Medicine 2001; 46:638–651.

[36] Fessler JA, Sutton BP. Nonuniform fast fourier transforms using min-max interpolation. Signal Processing, IEEE Transactions on 2003; 51:560–574.

[37] Bernstein MA, King KF, Zhou XJ, "Handbook of MRI Pulse Sequence". Elsevier Academic Press, MA, USA, 2004.

[38] Bernstein MA, Zhou XJ, Polzin JA, King KF, Ganin A, Pelc NJ, Glover GH. Concomitant gradient terms in phase contrast mr: Analysis and correction. Magnetic Resonance in Medicine 1998; 39:300–308.

[39] Papoulis A. Generalized sampling expansion. Circuits and Systems, IEEE Transactions on 1977; 24:652–654.

[40] Moriguchi H, Duerk JL. Bunched phase encoding (bpe): A new fast data acquisition method in mri. Magnetic Resonance in Medicine 2006; 55:633–648.

[41] GregoryMetzger XH. Application of interlaced fourier transform to echo-planar spectroscopic imaging. J Magn Reson 1997; 125:166–170.